Detection of *Karenia brevis* red tides on the West Florida Shelf using VIIRS observations: Accounting for spatial coherence with artificial intelligence

Yao Yao [a], Chuanmin Hu [a, *], Jennifer P. Cannizzaro [a], Brian B. Barnes [a], David C. English [a], Yuyuan Xie [a], Katherine Hubbard [b], Menghua Wang [c]

[a] College of Marine Science, University of South Florida, St. Petersburg, FL, USA

[b] Fish and Wildlife Research Institute, Florida Fish and Wildlife Conservation Commission, St. Petersburg, FL, USA

[c] National Oceanic and Atmospheric Administration, Center for Satellite Applications and Research, College Park, MD, USA

[*] Corresponding author: huc@usf.edu

Abstract

Harmful algal blooms (HABs) of the toxic dinoflagellate *Karenia brevis* occur annually on the West Florida Shelf (WFS). Detection of these blooms using satellite observations often suffers from two problems: lack of accurate algorithms to identify phytoplankton blooms in optically complex waters and patchiness (i.e., heterogeneity) of *K. brevis* during blooms. Here, using data collected by the Visible Infrared Imaging Radiometer Suite (VIIRS) on the Suomi National Polar-orbiting Partnership (SNPP) between 2017 and 2019, we develop a practical approach to overcome these difficulties despite the lack of a chlorophyll-a fluorescence band on VIIRS. The approach is based on artificial intelligence (specifically, a deep-learning convolutional neural network model), which uses spatial coherence of bloom patches to account for the patchiness of *K. brevis* concentrations. After proper training, the overall performance (i.e., F1 score) of the deep learning model is 89%. Extracted *K. brevis* patches were consistent with those derived from the Moderate Resolution Imaging Spectroradiometer (MODIS) on the Aqua satellite that has a fluorescence band. Furthermore, the wider swath of VIIRS over MODIS (3040-km *versus* 2330-km) led to more valid observations of bloom extent for improved near-real-time applications. The results not only demonstrate the capacity of VIIRS in HABs monitoring, but also show the value of the DL model in extracting *K. brevis* bloom patches for both near real-time applications and retrospective analysis.

Keywords: *Karenia brevis*, red tide, bloom detection, deep learning, remote sensing, VIIRS, MODIS

1. Introduction

Harmful algal blooms (HABs) are a global phenomenon that can negatively impact coastal ecosystems, economies, and human and wildlife health. Increases in HAB occurrences have been linked to eutrophication and climate change (Anderson et al., 2021; Fu et al., 2012; Glibert et al., 2014; Glibert & Burford, 2017). The primary HAB-forming species on the West Florida Shelf (WFS) is *Karenia brevis*, a toxic dinoflagellate that causes fish, seabird, and marine mammal mortalities and poses hazards to human and wildlife health (Fleming et al., 2007, 2011; Flewelling et al., 2005; Kirkpatrick et al., 2004; Steidinger, 2009). *K. brevis* blooms occur near-annually on the WFS, typically in late summer and fall, although particularly severe blooms have been reported year-round (e.g., 2005–2007, 2017–2019, and 2020–2021). The spatial scale of *K. brevis* blooms on the WFS also varies considerably from event to event and even over much shorter (i.e. daily) time scales. Areas with high concentrations of *K. brevis* are often called 'red tides', though these waters can appear in various shades of red, green, brown, or black.

The spatial and temporal variability of *K. brevis* blooms and associated impacts on the WFS require extensive monitoring to inform communication and forecasting. Water samples are routinely collected during field sampling of WFS coastal waters by the Florida Fish and Wildlife Conservation Commission (FWC) and dedicated research groups and volunteer networks, regardless of bloom conditions; additional sampling is also conducted in response to bloom events. Each year, thousands of samples are enumerated using microscopy to detect and monitor *K. brevis* and other HABs in Florida's (U.S.A.) marine and estuarine waters. This information is compiled within the FWC HAB Monitoring Database and reported by the FWC via regular updates on HABs. Background *K. brevis* concentrations (< 1,000 cells L^{-1}) are often observed in the non-bloom season_(Heil & Steidinger, 2009; Steidinger, 2009). When *K. brevis* cell counts exceed 1,000 cells L^{-1}, commercial shellfish harvesting areas may be closed due to potential hazards posed by the toxins. The lower limit for satellite detection is 50,000 cells L^{-1}, which is 1–2 orders of magnitude less than concentrations at which blooms are visible by the human eye (Tester & Steidinger, 1997). When cell counts are above 100,000 cells L^{-1}, reports of fish mortality and human respiration problems increase (Fleming et al., 2011; Flewelling et al., 2005; Kirkpatrick et al., 2004).

Over the past sixty years, more than a million water samples have been collected on the WFS and processed for *K. brevis* enumeration by FWC (FWC HAB Monitoring Database, 2021). However, the majority of samples were collected in nearshore waters, less than 10 km from the shoreline. This equates to fewer than one sample collected every two months within each 0.05° grid, although sampling intensity (including offshore) has increased substantially over time (Hu et al., 2022). Satellite remote sensing can help overcome the bias introduced by the scarcity of field data (especially offshore) because it provides increased synoptic spatial and temporal coverage (Amin, Zhou, et al., 2009; Amin et al., 2015; Esaias et al., 1998; Tester & Stumpf, 1998; Tomlinson et al., 2004). At elevated concentrations of *K. brevis*, water discoloration is captured in satellite images, and such a discoloration is often interpreted as an indication of *K. brevis* blooms (Cannizzaro et al., 2008, 2009; Cullen et al., 1997; Schofield et al., 1999; Tyler & Stumpf, 1989). Other factors, such as suspended sediments, colored dissolved organic matter (CDOM), and non-*K. brevis* phytoplankton blooms, can also cause water discoloration and be misconstrued as red tide (Dierssen et al., 2006). Blooms of *K. brevis* and other species may also occur at levels that can be observed via satellites but without discoloration observed with the naked eye. Thus, detection of *K. brevis* blooms using satellite observations requires algorithms, which are often empirical, to first detect phytoplankton blooms (Amin, Zhou, et al., 2009; Carvalho et al., 2010, 2011; El-Habashi et al., 2016; Hu & Feng, 2016; Qi et al., 2015; Stumpf et al., 2003; Tomlinson et al., 2009) and then distinguish the bloom types (e.g., *K. brevis*, diatom, *Pyrodinium bahamense*, *Tripos hircus*).

Satellite sensors equipped with spectral bands to measure solar-stimulated chlorophyll-a fluorescence, including the Moderate Resolution Imaging Spectroradiometer (MODIS) aboard Terra (2000–) and Aqua (2002–) and the Ocean and Land Colour Imager (OLCI) aboard Sentinel-3A (2016–) and Sentinel-3B (2018–), are used for bloom monitoring by U.S. Federal and State agencies (e.g., the U.S. National Oceanic and Atmospheric Administration (NOAA), https://coastalscience.noaa.gov/science-areas/habs/hab-forecasts/gulf-of-mexico/; FWC, https://myfwc.com/research/redtide/statewide/). Empirical algorithms developed using concurrent field and satellite data often rely on satellite-field matching pairs (i.e., data collected from the same location within a short time window), and thus can be regarded as ‘pixel-based’ approaches. These include techniques of the chlorophyll-a anomaly (Stumpf, 2001; Stumpf et al., 2003; Wang et al., 2021), particle backscattering coefficient b_{bp} ratio (Anderson et al., 2012; Cannizzaro et al., 2008; Carder et al., 1999; Morel, 1988), normalized water-leaving radiance (nL_w) ratio (Carvalho et al., 2011), nL_w spectral shape (Tomlinson et al., 2009), normalized Fluorescence Line Height (nFLH; Hu & Feng, 2016), Red Solar Induced Fluorescence (red SIF, Luis et al., 2023) and Red-Band Difference (RBD; Amin, Gilerson, et al., 2009; Amin, Zhou, et al., 2009). However, because *K. brevis* cell concentrations from adjacent waters (i.e., within a single pixel) can differ by several orders of magnitude (Tomlinson et al., 2009, also see supplemental Fig. S1), significant data spread is commonly observed when comparing satellite-estimated *K. brevis* concentration with water sample-determined *K. brevis* concentration (Hu & Feng, 2016).

The Visible Infrared Imaging Radiometer Suite (VIIRS) onboard the Suomi National Polar-orbiting Partnership (SNPP; 2011–), NOAA-20 (2017–), and NOAA-21 (2022–) exhibits similar spatial (375/750-m) and temporal (near-daily) resolutions as MODIS (250/500/1000-m) and OLCI (300-m), but VIIRS does not have the dedicated bands for measuring chlorophyll-a fluorescence for bloom detection (Hu et al., 2015). Despite this limitation, VIIRS has shown potential for bloom detection using alternative approaches, including the Red-Green Chlorophyll-a Index (RGCI; Qi et al., 2015) and neural network models (El-Habashi et al., 2016; El-Habashi & Ahmed, 2019). While bloom detection may be similar to nFLH and RBD, these algorithms were developed using pixel-based approaches without the ability to differentiate between *K. brevis* blooms and other types of blooms. Evaluation of these approaches using a large field dataset suggested that, although these approaches may work well for case studies, they are not applicable in a more general sense (supplemental Figs. S2 & S3).

Deep learning models are poised to overcome the limitations of pixel-based approaches by adding an emphasis on the recognition of spatial patterns. Also, unlike empirical approaches that typically utilize spectral information from only a few wavebands, these models can take advantage of the spectral information from all bands. Previous studies indicate the potential of using such approaches to identify HABs of *Magalefidinium polykrikoides* in Korean waters (Kim et al., 2019; Shin et al., 2022). However, for the *K. brevis* blooms on the WFS, there is no method for systematic observation using VIIRS data without a fluorescence band. With MODIS nearing the end of its lifespan (i.e., NASA will crease support of MODIS no later than 2026), the development of robust bloom detection algorithms for VIIRS sensors, scheduled for launch every five years, is critical to ensure a seamless satellite ocean color data record for monitoring HABs in near-real-time and documenting long-term trends. In order to address this need, the objective of this paper is to develop a practical approach to take advantage of computer artificial intelligence to recognize spatially coherent ocean color patterns in VIIRS imagery associated with *K. brevis* blooms.

2. Data and methods

2.1 *In-situ* data

Water samples from near-surface waters were used to determine the in-situ concentration of *K. brevis* at sampling sites. A total of 23,232 field data points for *K. brevis* cell counts were recorded at sample depths of ~ 0.5 m on the WFS from January 2017 to December 2019 (FWC HAB Monitoring Datbase, 2021). Fig. 1a shows the number of field *K. brevis* cell counts data in each 5-km grid. In this study, *K. brevis* cell counts larger than 100,000 cells L^{-1} are considered *K. brevis* blooms.

2.2 VIIRS satellite data

A total of 4,282 level-2 SNPP VIIRS granules covering the WFS from January 2017 to December 2019 were downloaded from the NOAA CoastWatch data portal (https://coastwatch.noaa.gov). These level-2 products included $nL_w(\lambda)$ for each band (410, 443, 486, 551, 638, and 671 nm) and quality assurance flag information. Default L3 flags developed by NOAA (Wang et al., 2017) were applied for quality control to exclude pixels with unreliable radiance values from further analysis. Fig. 1b shows the increased spatial and temporal coverage of VIIRS data compared to the *in-situ* cell count data.

Remote sensing reflectance ($R_{rs}(\lambda)$) for each band was determined from $nL_w(\lambda)$ as follows:

$$R_{rs}(\lambda) = nL_w(\lambda)/f_0(\lambda), \quad (1)$$

where $f_0(\lambda)$ is the mean extraterrestrial solar irradiance (Thuillier et al., 2003).

A cylindrical equidistant projection was used to map these data within the WFS at 1-km spatial resolution (Barnes et al., 2021). $R_{rs}(\lambda)$ data at 671-nm and 551-nm were used to generate the RGCI (Qi et al., 2015) following the equation:

$$RGCI = R_{rs}(671)/R_{rs}(551), \quad (2)$$

In addition, $R_{rs}(\lambda)$ at 551, 486, and 443 nm were used to generate Enhanced Red-Green-Blue (ERGB) composite images to show color patterns of coastal waters. The ERGB images differentiate dark features, caused by high absorption by chlorophyll-a and/or colored dissolved organic matter (CDOM), from bright features caused by either sediment resuspension or shallow bottom (Hu et al., 2005).

2.3 Deep learning model

Deep learning (DL) is a type of artificial intelligence that uses artificial neural networks with multiple layers to learn from data and make predictions. A Convolution Neural Network (CNN; Lecun et al., 1998) is a form of deep learning that is widely used in image segmentation for clustering parts of imagery together that belong to the same object class. Here, a type of CNN architecture called Res-Unet deep learning model (Diakogiannis et al., 2020; Qi et al., 2021; Wang & Hu, 2021; Xiao et al., 2018; Yao et al., 2023) is used. This model combines constructions inherent to both Res-Net (He et al., 2016) and U-net (Ronneberger et al., 2015) models, thus improving ability to effectively perform image segmentation tasks.

The workflow in this study follows three main steps (Fig. 2). First, a set of "ground truth" images were prepared semi-objectively and combined with satellite $R_{rs}(\lambda)$ and RGCI for model training. Here, the term "ground truth" refers to the information determined by integrating ground (i.e., field) measurements and image analysis results as opposed to either ground measurements alone or the theoretical "truth". The trained model was then validated using a separate set of "ground truth" images that were reserved for evaluation. Finally, the model was applied to VIIRS data from 2017–2019, and the model output was used to generate monthly statistics to examine spatiotemporal variability of *K. brevis* blooms over the course of the bloom event.

2.3.1 "Ground truth" image preparation

K. brevis blooms exhibit high RGCI (Qi et al., 2015) and appear reddish-black in ERGB composite imagery (Hu et al., 2005), allowing these patches to be differentiated from the surrounding waters. However, not all patches with high RGCI are *K. brevis* blooms because blooms of other phytoplankton can also lead to high RGCI values, and other factors (e.g., CDOM) can cause ERGB images to appear reddish black. Here, field sample data are used to confirm that patches with high RGCI are *K. brevis* blooms. The patches were identified as *K. brevis* only if the field data showed high *K. brevis* cell counts (> 100,000 cells L^{-1}) that corresponded to high RGCI and reddish-blackish features in ERGB. This practice has been employed before to delineate *K. brevis* blooms using field sample data and MODIS/Aqua RBD images (Hu et al., 2022).

Based on the criteria above, "ground truth" images were prepared as demonstrated in Fig. 3 using the following steps:

1. *K. brevis* cell counts data (± 7 days) were overlaid on VIIRS daily (i.e., snapshot) RGCI and ERGB composite imagery (Figs. 3a & 3b).
2. Patches associated with *K. brevis* cell counts > 100,000 cells L^{-1} that exhibit high RGCI and appear reddish black in the ERGB imagery were roughly outlined manually using the ENVI/IDL region of interest (ROI) tool (Fig. 3b).
3. Pixels within the outline with RGCI ≥ the threshold of RGCI (T_{RGCI}) (e.g., *K. brevis* bloom) were considered as bloom pixels and extracted objectively (Fig. 3c). T_{RGCI} was set as 0.22, which corresponds to a chlorophyll-a concentration of 1.5 μg L^{-1} and approximately 150,000 *K. brevis* cells L^{-1} (Qi et al., 2015; Stumpf et al., 2003; Tester et al., 2008). This threshold is consistent with that used for the MODIS RBD by Hu et al. (2022).
4. The bloom pixels were assigned a value of 1. All remaining pixels, including those outside the outline or with RGCI < T_{RGCI}, were assigned a value of 0 (e.g., non-*K. brevis* bloom) or NaN (not a number, due to no observation or invalid pixels) (Fig. 3d).

A total of 100 VIIRS images were delineated following the above steps. Twenty three of these images contained high VIIRS RGCI with *K. brevis* cell counts equal to zero and are intended to help prevent false positives. Through random selection, 47 of these images were designated for training, and the remaining 53 images were reserved for validation. Here, although the cell counts data were likely collected not in the same day of the image acquisition and water could have moved within ± 7 days to cause a mismatch between the locations of the *in situ* data and image feature, as long as there were high cell counts within or near an image feature, the feature is delineated as a *K. brevis* bloom patch. This is also one reason why a patch-wise approach should work better than a pixel-wise approach.

2.3.2 Model training

A total of 47 "ground truth" images and their corresponding $R_{rs}(\lambda)$ and RGCI data were used as a training dataset for developing and training the DL model. To balance the weight of the input data and make the deep learning model training converge smoothly, each $R_{rs}(\lambda)$ band (410, 443, 486, 551, 638, 671 nm) was normalized by:

$$nR_{rs}(\lambda) = (\log(R_{rs}(\lambda)) - \log(R_{rs}(\lambda)_{min}))\ /(\log(R_{rs}(\lambda)_{max}) - \log(R_{rs}(\lambda)_{min})), \quad (3)$$

where $R_{rs}(\lambda)_{min}$ and $R_{rs}(\lambda)_{max}$ were determined to be 0.0001 and 0.02 by trial and error, respectively. If $R_{rs}(\lambda)$ was less than 0.0001, it was set to 0.0001; and if $R_{rs}(\lambda)$ was great than 0.02, it was set to 0.02.

Likewise, RGCI was normalized as follows:

$$nRGCI = (RGCI - RGCI_{min})\ /\ (RGCI_{max} - RGCI_{min}), \quad (4)$$

where RGCI_{min} and RGCI_{max} were determined to be 0.1 and 1.5 by trial and error, respectively. If RGCI was less than 0.1, it was set to 0.1; and if RGCI was greater than 1.5, it was set to 1.5.

Squared convolution kernels were applied in this training network. Thus, each input training image was divided into several spatially non-overlapping sub-images of 256 × 256 pixels, with the sub-image size determined by computing power. Each sub-image was then used to train the DL model, and the Jaccard distance index was used to assess the model convergence. After passing through the deep convolutional layers, the model can recognize the characteristic $R_{rs}(\lambda)$ spectral shapes of *K. brevis* bloom patch and the coherent spatial relationships among the $R_{rs}(\lambda)$ spectral features that help identify the *K. brevis* bloom patches.

2.3.3 Model validation

A total of 53 delineated VIIRS "ground truth" images were reserved for validation to evaluate the model performance. The morphology of each patch in the model extracted images was visually compared with the semi-objectively delineated patches of the "ground truth" images and field *K. brevis* cell concentration data to determine whether the model extracted results matched those from the "ground truth" images. A confusion matrix (Stehman, 1997) was used to report the number of true-positives (TP), true-negatives (TN), false-positives (FP), and false-negatives (FN), as well as the F1 score to evaluate the overall accuracy. The F1 score was calculated as:

$$F1 = 2TP \,/\, (2TP + FP + FN) \times 100\%. \quad (5)$$

The above statistics is based on the evaluation of the 53 image pairs, each containing a "ground truth" image (or truth image) and an image of model results (or model image). There are 41 *K. brevis* bloom truth images and 12 non-bloom truth images. Each model image was compared to its corresponding truth image to determine whether the model image is a TP, TN, FP, or FN. A model image is a TP if 1) the morphology of each bloom patch in the model image matches that in the truth image and 2) the overlapping bloom area (as measured by the number of pixels) between the model image and the truth image is > 75% of the bloom area in the truth image, otherwise the model image is an FN. A model image is an FP if any patch is classified as a bloom patch, but the corresponding truth image shows no bloom, otherwise the model image is an TN.

In addition to the confusion matrix, the bloom areas of all image pairs (i.e., the truth images and the model images) were compared using a linear fitting with the coefficient of determination (R^2) and the root mean square error (RMSE). RMSE was calculated as follows:

$$RMSE = \sqrt{\frac{1}{n}\sum_{i=1}^{n}\left(\frac{x_i - \hat{x}_i}{\hat{x}_i}\right)^2} \times 100\%, \quad (6)$$

where x_i is the bloom area (i.e., number of pixels) of the model extracted result of the i-th model image, and $\hat{x}_i$ is the area of the i-th truth image.

Spectral similarities between $R_{rs}(\lambda)$ measured in *K. brevis* bloom and non-*K. brevis* bloom patches were examined using the Spectral Angle Mapper (SAM) index (Kruse et al., 1993). The SAM (in degrees) indicates the spectral similarity between two $R_{rs}(\lambda)$ spectra by calculating the angle between them. The closer SAM is to 0-degree, the greater the similarity between the two spectral shapes.

2.3.4 Statistics of K. brevis coverage

After the model was trained and validated, it was applied to a 3-year series of VIIRS data (2017–2019) that encompassed a long-lasting *K. brevis* bloom event. Each pixel was classified into one of three classes: '*K. brevis* bloom' with a value of 1, 'non-*K. brevis* bloom' with a value of 0, or 'no valid observation'. The 'no valid observation' class was determined using the default L3 quality assurance flag information processed by NOAA (Wang et al., 2017), and these pixels were excluded from the following statistics.

Monthly maps of bloom occurrence frequency (BOF) were generated from the individual classified images and for a given location were calculated as follows:

$$BOF = (N_{kb}/(N_{kb} + N_{nkb})) \times 100\%, \quad (7)$$

where N_{kb} is the total number of '*K. brevis* bloom' pixels and N_{nkb} is the total number of 'non-*K. brevis* bloom' pixels. To make the statistics more meaningful, pixels with fewer than five valid observations (see definition above) in any given month were excluded. Bloom areal footprints were then calculated from all > 0% pixels in the monthly BOF maps.

Monthly BOF maps were also generated from individual classified maps derived based on RGCI > T_{RGCI} and chlorophyll-a > 1.5 μg L^{-1} derived using a neural network model (El-Habashi et al., 2016) to compare with model results.

2.4 MODIS-based *K. brevis* bloom occurrence frequency maps

MODIS/Aqua data were used to qualitatively assess the VIIRS deep learning model results. Specifically, *K. brevis* blooms were classified following the work of Hu et al. (2022) by integrating water sample data and MODIS data. Briefly, field *K. brevis* cell counts were first overlaid on MODIS RBD (Amin et al., 2015; Amin, Zhou, et al., 2009). Patches with high RBD and high field *K. brevis* cell concentrations were delineated semi-objectively: a crude outline was manually drawn over each patch, and pixels within the outline with RBD > 0.15 mW cm^{-2} μm^{-1} sr^{-1} (which corresponds to 150,000 cells L^{-1}, Hu & Feng, 2016) were identified as *K. brevis* bloom pixels. Monthly BOF maps were generated from the daily imagery similarly to VIIRS (Section 2.3.4).

3. Results

3.1 Model validation

A confusion matrix for assessing the performance of the DL model is shown in Table 1. The overall F1 score was 89% with an accuracy of 81% and precision of 83%. Four sets of example images from the validation dataset are presented in Fig. 4, showcasing TP, TN, FP, and FN results. The first set of images in the top row displays the TP results where the DL model successfully extracted *K. brevis* patches that match the “ground truth” image. Here, each TP case meets the criteria of both morphological evaluation and 75% threshold of bloom area as described in the methodology above. Of the 39 TP cases, the ratio of the overlapping bloom area to the true bloom area for each image pair ranged between 77.7% and 96.3%, with an overall ratio of 82.2% when all image pairs were combined. The second set of images illustrates the TN results where the DL model correctly identified non-*K. brevis* bloom (i.e., not a single patch was a bloom patch in both the “ground truth” image and the model image). The third set of images presents the FP results where the DL model extracted incorrect bloom patches, and the fourth set of images displays the FN results where the DL model failed to identify > 25% of the overlapping bloom areas between the “ground truth” image and the model image.

Table 1. Performance evaluation of the DL model where P and PP are the number of “true” and predicted *K. brevis* blooms, respectively; N and PN are the number of “true” and predicted non-*K. brevis* bloom, respectively. TN and TP are the number of true negatives and positives, respectively; FN and FP are the number of false negatives and positives, respectively.

Total n = **53**		Predicted		F1 score	2TP/(2TP+FP+FN)	88.6%
		PP	PN			
“Ground truth”	P	TP **39**	FN **2**	True positive rate (TPR)	TP/(TP+FN)	95.1%
	N	FP **8**	TN **4**	False positive rate (FPR)	FP/(FP+TN)	66.7%
Precision	TP/(TP+FP)	83.0%		Accuracy	(TP+TN)/n	81.1%

A comparison between bloom areas (in number of pixels) determined from the “ground truth” images and the corresponding model images is presented in Fig. 5, wherein the overall RMSE was found to be 31.5%, and the coefficient of determination R^2 was calculated to be 0.92. Bloom areal extent was underestimated by the model in the Panhandle region in late-2018. These results will be discussed in detail below.

3.2 Model performance

The DL model, trained and verified based on the VIIRS spectral information and image coherent context, can identify the *K. brevis* patches and distinguish them from non-*K. brevis* bloom patches.

Fig. 6 shows a VIIRS scene collected on 16 September 2018 that contains two separate patches of high RGCI water that appear darkish red in the ERGB imagery. *K. brevis* cell counts > 100,000 cells L^{-1} confirm that the northern patch offshore of Charlotte Harbor was a true bloom, and the model correctly identified this bloom patch. Background cell counts (<1,000 cells L^{-1}) were collected in the more southerly patch located south of Cape Romano (~26°N), and the model correctly identified this patch as a non-*K. brevis* bloom. VIIRS $R_{rs}(\lambda)$ spectral shapes were examined in Fig. 6a at locations within these patches. The high similarity in spectral shape (SAM = 4.94°) indicates that both patches would be categorized as *K. brevis* blooms based on RGCI alone. The DL model accurately differentiated between the *K. brevis* bloom patch and the non-*K. brevis* bloom patches.

Fig. 7 further demonstrates how the VIIRS DL model generates fewer false-positive classifications compared to both RGCI (Qi et al., 2015) and the neural network model (El-Habashi et al., 2016). Monthly BOF maps using all three techniques were generated during a *K. brevis* bloom event (August 2018) and non-*K. brevis* bloom event (June 2019), and are compared to monthly FWC cell abundance data. While the neural network and RGCI retrieval results accurately detect the *K. brevis* bloom in the central WFS in August 2018, there are some false-positive results in nearshore waters to the north in the Panhandle/Big Bend regions and south of Cape Romano (~26° N). False positive classifications were also prevalent in these regions during the non-*K. brevis* bloom event in June 2019. The VIIRS DL model, on the other hand, shows strong consistency with *K. brevis* cell abundance, indicating improved performance in accurately identifying both *K. brevis* blooms and non-blooms.

3.3 Comparisons between VIIRS and MODIS

Monthly MODIS BOF maps generated by semi-objective delineation for May 2018 to January 2019 were previously presented by Hu et al. (2022). In Fig. 8, comparisons are made between bloom footprints generated from these maps and those derived using the VIIRS DL model. *K.*

brevis blooms were detected by both methods from June 2018 to January 2019, but several differences were observed in the footprint areas. The VIIRS DL model often estimated *K. brevis* blooms extending further into shallow coastal waters than the MODIS BOF, resulting in larger footprint areal estimates than those observed with MODIS, except for cases during October and November 2018 when MODIS derived BOF footprints were larger than those from VIIRS in the Panhandle and Big Bend regions.

Fig. 9 provides a detailed visualization of the differences in bloom footprint observed between VIIRS and MODIS for imagery acquired approximately one hour apart on October 30, 2018. The VIIRS bloom footprint was 44% lower than that from MODIS. While MODIS RBD was well above the threshold used by Hu et al. (2022) for identifying bloom patches, VIIRS RGCI was close to the bloom threshold used when training the model. Residual increased suspended sediment following the recent passage of a winter frontal system is evident in the VIIRS ERGB and may explain why VIIRS failed to detect this patch. VIIRS and MODIS $R_{rs}(\lambda)$ spectra extracted from within the bloom patch are similar (SAM = 9.07°).

4. Discussion

4.1. Strengths and limitations

K. brevis blooms on the WFS pose threats to coastal ecosystems and public health and can negatively impact local economies. An accurate means for near-real-time monitoring is required to help protect public health, and long-term monitoring is needed to better understand the underlying causes of blooms and identify bloom trends. Field measurements of *K. brevis* cell counts are highly precise; however, their limited spatial and temporal resolutions restrict their overall efficacy in consistently monitoring blooms with accuracy. Remote sensing may serve as a valuable tool to complement field-based monitoring programs. However, previous remote sensing algorithms often rely on pixel-based approaches with pre-determined thresholds applied to identify blooms for each pixel with an image (Amin, Zhou, et al., 2009; Cannizzaro et al., 2008, 2009; Carvalho et al., 2010, 2011; Hu & Feng, 2016; Qi et al., 2015; Soto et al., 2015; Stumpf et al., 2003; Tomlinson et al., 2009). These had limited success due to the problems associated with sub-pixel variability (Hu & Feng, 2016; Fig. S1). While neural network models (El-Habashi et al., 2016; El-Habashi & Ahmed, 2019) offer several advantages over threshold-based empirical approaches, systemic testing showed unsatisfactory performance (Figs. S2 & S3). Here, we developed a deep learning model for detecting *K. brevis* blooms on the WFS using VIIRS imagery that outperforms these other methods.

By adopting a patch-wise approach that considers spatial information (He et al., 2016), the VIIRS DL model can overcome limitations associated with subpixel variability that are inherent in pixel-wise approaches (Hu & Feng, 2016; Fig. S1). Furthermore, unlike empirical algorithms using a few bands, such as the RGCI (Qi et al., 2015) and RBD (Amin, Zhou, et al., 2009) algorithms, the VIIRS DL model utilizes all VIIRS bands as data input and relies on $R_{rs}(\lambda)$ spectral shapes for bloom identification. This spectral data from all bands can provide more comprehensive information compared to the limited utilization of just two or three bands in other empirical algorithms, therefore improving the accuracy of the deep learning model (Krizhevsky et al., 2017).

As an automated patch-wise approach, the VIIRS DL model reduces false positives and improves *K. brevis* bloom patch delineation, thus reducing the need for secondary verification by *in situ* data and/or human interpretation. In contrast, most traditional approaches first determine chlorophyll-a concentrations or a bloom patch (El-Habashi et al., 2016; Hu et al., 2005; Soto et al., 2015), and then use in-situ sampling and/or human interpretation to confirm whether the bloom patch is due to *K. brevis* or other phytoplankton. However, this does not indicate that the DL model does not require *in situ* data for verification, particularly because *K. brevis* is not the only dinoflagellate and blooms of other dinoflagellates may have similar optical properties to be detected by the same DL model. If this is the case, what the DL model detects are blooms of dinoflagellates. Yet because *K. brevis* is the dominant dinoflagellate to cause red tides, one can assume that most of the detected blooms are likely due to *K. brevis*.

Furthermore, VIIRS has a wider swath width (3040-km) compared with MODIS (2330-km), which means VIIRS has a greater number of observations to compare. Fig. 10 compares the monthly coverage and the number of valid observations for MODIS and VIIRS during the latter part of the 2017–2019 HABs bloom event (July 2018–December 2018). Although MODIS and VIIRS had similar *K. brevis* bloom trends, there were differences in the number of valid observation numbers. VIIRS had an average of ten or more valid observations per pixel per month in the WFS region, while MODIS had only around five. Under good observation conditions (e.g., cloud-free and optimal solar/sensor zenith angles), as in October 2018, VIIRS could achieve more than 25 valid observations in the offshore area of Florida, while MODIS had only about 15.

Additionally, unlike MODIS that saturates its fluorescence band (678-nm) over moderate to high sun glint (Hu et al., 2012), VIIRS does not saturate under such conditions. Fig. 11 displays a case study where a 5-day period of VIIRS and MODIS observations showed the advantage of using VIIRS data for near-real-time monitoring. Due to the land adjacency effect, the saturation of the fluorescence band, and the narrower swatch (than VIIRS), MODIS had only three images showing scattered *K. brevis* patches during the 5-day period, with none of them capturing the full extent of the bloom. In contrast, VIIRS had at least one image per day in this 5-day period, with each of them showing near-complete bloom extent, which has extensive value toward guiding timely and targeted resource management and public health communications during *K. brevis* blooms.

Despite the advantages of using a deep learning model with VIIRS observation to detect *K. brevis* blooms, there are several limitations. One is the definition of "bloom". Here, the dataset used to train the VIIRS DL model was prepared based on the RGCI threshold corresponding to 150,000 cells L^{-1} of *K. brevis* (Amin et al., 2015; Amin, Zhou, et al., 2009; Hu et al., 2022; Hu & Feng, 2016; Qi et al., 2015; Soto et al., 2015) if the phytoplankton population is dominated by *K. brevis*. Because of the significant bloom patchiness (Fig. S1) and because of mixed phytoplankton assemblage, this definition does not indicate that within a delineated bloom patch, *K. brevis* cell concentration is always > 150,000 cells L^{-1}. As shown in Fig. 3, cell concentration within the bloom patch can be much lower than this threshold, and sometimes can be 0 – 1,000. This certainly does not mean that a *K. brevis* bloom patch with maximum concentration of ~10,000 cells L^{-1} (or even ~5,000 cells L^{-1}) can be detected by the DL model. What it means is that an image feature with maximum cell counts lower than this threshold is considered as "non-bloom" in the training and validation datasets. However, this threshold is higher than the threshold of 5,000 cells L^{-1} when the commercial shellfish harvesting areas were previously required to be closed. It is also higher than the cell count threshold above which fish mortality and human respiration irritation often occur (Fleming et al., 2011; Flewelling et al., 2005; Kirkpatrick et al., 2004). Correspondingly, the *K. brevis* blooms detected here are rather conservative, i.e., without including bloom patches (or other image features) with maximum *K. brevis* concentrations lower than this threshold, although these waters are also harmful to marine animals. Also, bloom detection is currently a binary classification that only allows for a distinction between the presence and absence of blooms without quantifying the intensity of them, although such a quantification may be possible when taking account of the RGCI values of the delineated bloom patches. Clearly, future efforts are required to detect blooms at lower *K. brevis* concentrations and to quantify the concentrations beyond presence/absence detections. This would improve the utility of the tool for tracking bloom transport, evolution, and appearance/disappearance.

The second limitation relates to the VIIRS DL model's applicability even under cloud free conditions. Similar to other satellite sensors, the DL model is not applicable to image pixels immediately adjacent to land because these pixels may be mixed pixels (between water and land) or contaminated by land adjacency effect. In this study, a 2-pixel buffer was applied immediately adjacent to land, effectively masking those areas. Estuaries were also masked to eliminate the influence of land adjacency effects. Furthermore, the strength of avoiding false-positive detection in sediment-rich waters (because of the use of the full $R_{rs}(\lambda)$ spectral information together with spatial context) can become a weakness in some special cases. For example, if sediment resuspension, due to the passage of cold fronts or storms, occurs during a *K. brevis* bloom, the high concentrations of sediment particles can obscure the *K. brevis* signals, leading to no bloom detection. Fig. 12 shows such a case. The ERGB images in Fig. 12a and Fig. 12c, overlaid with field-measured *K. brevis* cell counts, reveal that in the Epicenter region, there was a persistent and expansive *K. brevis* bloom during mid-November 2018, and the bloom patches were correctly extracted by the VIIRS DL model (Figs. 12d and 12f). During this period and on 16 November 2018, a cold front passed through the Epicenter region, causing high concentrations of resuspended sediment particles (bright features in Fig. 12b), which led to no bloom detection (Fig. 12e). However, such a false-negative detection can be easily remedied by inspecting sequential images: if similar bloom patches are detected in t1 and t3 but not in t2 when sediment resuspension occurs, one can safely assume that similar bloom patches still exist in t2. Likewise, for near-real-time applications, if bloom patches are found in t1, the lack of detected bloom patches in t2 due to sediment resuspension does not indicate the end of the bloom.

Therefore, the lack of ability to detect *K. brevis* blooms in sediment-rich waters is much less of a problem than the false-positive detections in sediment-rich waters by other methods.

4.2. Future perspective

VIIRS measurements used in this study are from the SNPP satellite, yet the same sensor is also carried by the NOAA-20 (2017–present) and NOAA-21 (2022–present) satellites. Future satellites carrying the same VIIRS are expected to be launched about every 5 years. A combination of these sensors, each with a different equatorial crossing time, can provide multiple observations of *K. brevis* blooms in a single day. This will not only improve the cloud-free data coverage, but also may provide more than one observation per day to capture the diel vertical migration of *K. brevis* cells (Arnone et al., 2017; Hu, Barnes, et al., 2016; Qi et al., 2017; Schofield et al., 2006). Likewise, the multi-sensor observations can not only help to study the timing, intensity, and short-term dynamics of *K. brevis* blooms, but also improve near-real-time observations to alert the public on bloom situations (e.g., NOAA's HAB Forecast System, or the Integrated Redtide Information System (IRIS), Hu, Murch, et al., 2016; https://optics.marine.usf.edu/projects/iris.html). The same logic can be extended to other sensors such as the Ocean and Land Colour Instrument (OLCI) on the Sentinel-3A (2016–present) and Sentinel-3B (2018–present) satellites. While cross-sensor consistency is yet to be determined, the integration of these different satellite sensors can provide more comprehensive and accurate observations of *K. brevis* blooms than being offered by any single sensor, thus facilitating both research on bloom dynamics and near-real-time monitoring.

The findings here demonstrate the success of combining VIIRS observations and computer artificial intelligence to detect HABs, while near-real-time applications require implementation of this approach to generate *K. brevis* bloom maps automatically, so these maps can be incorporated in the current IRIS. We expect to implement this approach in IRIS to monitor *K. brevis* blooms in near-real-time in the next step.

Finally, the demonstration is for *K. brevis* blooms on the WFS between 2017 and 2019. Can the same DL model be applied to other years for the same WFS and to other regions in the Gulf of Mexico (GoM) where *K. brevis* have also been reported (e.g., coastal waters off Texas)? Because the DL model is strictly data driven, if the training used here for the period of 2017 – 2019 does not encompass all observing scenarios (e.g., solar/viewing geometry, weak-moderate sun glint, different aerosol types and thicknesses) and all optical complexity (e.g., optically shallow bottom, non-algal water constituents) for other years or for other GoM regions, then the DL model needs to be retrained to include those scenarios. Otherwise, there is no need for retraining. For these reasons, because a 3-year observing period is believed to be long enough to cover all possible observing scenarios, application of the DL model for the WFS but to other years is unlikely to require retraining. In contrast, for other regions of the GoM, because the reasons leading to optical complexity may be different, a retraining is very likely needed. For the same reason, because HABs are a global phenomenon (Anderson et al., 2021) and because of the global coverage of VIIRS and other satellite data, we expect that such a machine learning approach may find more applications in other regions where HABs also occur, once field data are available for training and validation. These HABs are not necessarily caused by *K. brevis*, but can be caused by other dinoflagellates. In particular, future satellite missions will have the capacity to collect hyperspectral data on both sun-synchronous and geostationary satellite platforms. These include NASA's Plankton, Aerosol, Cloud, ocean Ecosystem (PACE) mission, NASA's Geostationary Littoral Imaging and Monitoring Radiometer (GLIMR) mission, and NOAA's Geostationary Extended Observations (GeoXO) mission. These missions will provide unprecedented ocean color data to bolster the ability to detect HABs by accounting for spatial coherence, spectral contrasts, and short-term changes.

5. Conclusion

To date, compared with MODIS or OLCI, the use of VIIRS in detecting HABs in the Gulf of Mexico is limited, possibly due to its lack of a fluorescence band. This technical challenge is circumvented here through the use of full spectral information from each VIIRS image pixel and a deep learning model to account for the spatial context of bloom pixels. Such an approach detects *K. brevis* blooms on the West Florida Shelf as spatially coherent features, thus avoiding typical problems of *K. brevis* patchiness (i.e., heterogeneity) encountered by traditional pixel-based methods. The approach led to detected *K. brevis* bloom patterns that are consistent with those derived from MODIS and microscopy observations and, meanwhile, the wide swath makes VIIRS particularly useful in both retrospective analyses of bloom dynamics and near-real-time monitoring of bloom occurrence. We expect to implement such an approach for near-real-time data production in the current IRIS.

6. Acknowledgements

This work was supported by the Florida Fish and Wildlife Conservation Commission (FWC, Agreement No. 20035), the U.S. NASA GLIMR program (80LARC21DA002, Subcontract # L0141 through University of New Hampshire), the NASA Water Resources program (80NSSC19K1200), and by the JPSS/NOAA ocean color cal/val program (ST13301CQ0050/1332KP22FNEED004). We thank NOAA and NASA for providing VIIRS and MODIS data, respectively. We also thank the FWC-Fish and Wildlife Research Institute's Harmful Algal Bloom team for providing *K. brevis* cellular abundance data. Two anonymous reviewers provided extensive comments and suggestions to improve the presentation of this work, whose efforts are appreciated. The scientific results and conclusions, as well as any views or opinions expressed herein, are those of the author(s) and do not necessarily reflect those of NOAA or the Department of Commerce.

Reference

Amin, R., Gilerson, A., Gross, B., Moshary, F., & Ahmed, S. (2009). MODIS and MERIS detection of dinoflagellates blooms using the RBD technique. *Remote Sensing of the Ocean, Sea Ice, and Large Water Regions 2009*, *7473*, 33–43. https://doi.org/10.1117/12.830631

Amin, R., Penta, B., & deRada, S. (2015). Occurrence and spatial extent of HABs on the West Florida Shelf 2002–present. *IEEE Geoscience and Remote Sensing Letters*, *12*(10), 2080–2084. https://doi.org/10.1109/LGRS.2015.2448453

Amin, R., Zhou, J., Gilerson, A., Gross, B., Moshary, F., & Ahmed, S. (2009). Novel optical techniques for detecting and classifying toxic dinoflagellate *Karenia brevis* blooms using satellite imagery. *Optics Express*, *17*(11), 9126. https://doi.org/10.1364/OE.17.009126

Anderson, D. M., Alpermann, T. J., Cembella, A. D., Collos, Y., Masseret, E., & Montresor, M. (2012). The globally distributed genus *Alexandrium*: Multifaceted roles in marine ecosystems and impacts on human health. *Harmful Algae*, *14*, 10–35. https://doi.org/10.1016/j.hal.2011.10.012

Anderson, D. M., Fensin, E., Gobler, C. J., Hoeglund, A. E., Hubbard, K. A., Kulis, D. M., Landsberg, J. H., Lefebvre, K. A., Provoost, P., & Richlen, M. L. (2021). Marine harmful algal blooms (HABs) in the United States: History, current status and future trends. *Harmful Algae*, 101975.

Arnone, R. A., Vandermeulen, R. A., Soto, I. M., Ladner, S. D., Ondrusek, M. E., & Yang, H. (2017). Diurnal changes in ocean color sensed in satellite imagery. *Journal of Applied Remote Sensing*, *11*(3), 032406. https://doi.org/10.1117/1.JRS.11.032406

Barnes, B. B., Hu, C., Bailey, S. W., Pahlevan, N., & Franz, B. A. (2021). Cross-calibration of MODIS and VIIRS long near infrared bands for ocean color science and applications. *Remote Sensing of Environment*, *260*, 112439. https://doi.org/10.1016/j.rse.2021.112439

Cannizzaro, J. P., Carder, K. L., Chen, F. R., Heil, C. A., & Vargo, G. A. (2008). A novel technique for detection of the toxic dinoflagellate, *Karenia brevis*, in the Gulf of Mexico from remotely sensed ocean color data. *Continental Shelf Research*, *28*(1), 137–158. https://doi.org/10.1016/j.csr.2004.04.007

Cannizzaro, J. P., Hu, C., English, D. C., Carder, K. L., Heil, C. A., & Müller-Karger, F. E. (2009). Detection of *Karenia brevis* blooms on the west Florida shelf using in situ backscattering and fluorescence data. *Harmful Algae*, *8*(6), 898–909. https://doi.org/10.1016/j.hal.2009.05.001

Carder, K. L., Chen, F. R., Lee, Z. P., Hawes, S. K., & Kamykowski, D. (1999). Semianalytic Moderate-Resolution Imaging Spectrometer algorithms for chlorophyll *a* and absorption with bio-optical domains based on nitrate-depletion temperatures. *Journal of Geophysical Research: Oceans*, *104*(C3), 5403–5421. https://doi.org/10.1029/1998JC900082

Carvalho, G. A., Minnett, P. J., Banzon, V. F., Baringer, W., & Heil, C. A. (2011). Long-term evaluation of three satellite ocean color algorithms for identifying harmful algal blooms (Karenia brevis) along the west coast of Florida: A matchup assessment. *Remote Sensing of Environment*, *115*(1), 1–18. https://doi.org/10.1016/j.rse.2010.07.007

Carvalho, G. A., Minnett, P. J., Fleming, L. E., Banzon, V. F., & Baringer, W. (2010). Satellite remote sensing of harmful algal blooms: A new multi-algorithm method for detecting the

Florida Red Tide (*Karenia brevis*). *Harmful Algae*, *9*(5), 440–448. https://doi.org/10.1016/j.hal.2010.02.002

Cullen, J. J., Ciotti, Á. M., Davis, R. F., & Lewis, M. R. (1997). Optical detection and assessment of algal blooms. *Limnology and Oceanography*, *42*(5part2), 1223–1239. https://doi.org/10.4319/lo.1997.42.5_part_2.1223

Diakogiannis, F. I., Waldner, F., Caccetta, P., & Wu, C. (2020). ResUNet-a: A deep learning framework for semantic segmentation of remotely sensed data. *ISPRS Journal of Photogrammetry and Remote Sensing*, *162*, 94–114. https://doi.org/10.1016/j.isprsjprs.2020.01.013

Dierssen, H. M., Kudela, R. M., Ryan, J. P., & Zimmerman, R. C. (2006). Red and black tides: Quantitative analysis of water-leaving radiance and perceived color for phytoplankton, colored dissolved organic matter, and suspended sediments. *Limnology and Oceanography*, *51*(6), 2646–2659. https://doi.org/10.4319/lo.2006.51.6.2646

El-Habashi, A., & Ahmed, S. (2019). Analyses of satellite ocean color retrievals show advantage of neural network approaches and algorithms that avoid deep blue bands. *Journal of Applied Remote Sensing*, *13*(02), 1. https://doi.org/10.1117/1.JRS.13.024509

El-Habashi, A., Ioannou, I., Tomlinson, M., Stumpf, R., & Ahmed, S. (2016). Satellite retrievals of *Karenia brevis* Harmful Algal Blooms in the west Florida Shelf using neural networks and comparisons with other techniques. *Remote Sensing*, *8*(5), 377. https://doi.org/10.3390/rs8050377

Esaias, W. E., Abbott, M. R., Barton, I., Brown, O. B., Campbell, J. W., Carder, K. L., Clark, D. K., Evans, R. H., Hoge, F. E., Gordon, H. R., Balch, W. M., Letelier, R., & Minnett, P. J.

(1998). An overview of MODIS capabilities for ocean science observations. *IEEE Transactions on Geoscience and Remote Sensing*, *36*(4), 1250–1265. https://doi.org/10.1109/36.701076

Fleming, L. E., Kirkpatrick, B., Backer, L. C., Bean, J. A., Wanner, A., Reich, A., Zaias, J., Cheng, Y. S., Pierce, R., Naar, J., Abraham, W. M., & Baden, D. G. (2007). Aerosolized Red-Tide Toxins (Brevetoxins) and Asthma. *Chest*, *131*(1), 187–194. https://doi.org/10.1378/chest.06-1830

Fleming, L. E., Kirkpatrick, B., Backer, L. C., Walsh, C. J., Nierenberg, K., Clark, J., Reich, A., Hollenbeck, J., Benson, J., Cheng, Y. S., Naar, J., Pierce, R., Bourdelais, A. J., Abraham, W. M., Kirkpatrick, G., Zaias, J., Wanner, A., Mendes, E., Shalat, S., … Baden, D. G. (2011). Review of Florida red tide and human health effects. *Harmful Algae*, *10*(2), 224–233. https://doi.org/10.1016/j.hal.2010.08.006

Flewelling, L. J., Naar, J. P., Abbott, J. P., Baden, D. G., Barros, N. B., Bossart, G. D., Bottein, M.-Y. D., Hammond, D. G., Haubold, E. M., Heil, C. A., Henry, M. S., Jacocks, H. M., Leighfield, T. A., Pierce, R. H., Pitchford, T. D., Rommel, S. A., Scott, P. S., Steidinger, K. A., Truby, E. W., … Landsberg, J. H. (2005). Red tides and marine mammal mortalities. *Nature*, *435*(7043), 755–756. https://doi.org/10.1038/nature435755a

Fu, F., Tatters, A., & Hutchins, D. (2012). Global change and the future of harmful algal blooms in the ocean. *Marine Ecology Progress Series*, *470*, 207–233. https://doi.org/10.3354/meps10047

FWC HAB Monitoring Database. (2021). *Fish and wildlife conservation commission. HAB monitoring database* [Data set]. https://myfwc.com/research/redtide/monitoring/database/ *Accessed on July 30, 2021.*

Glibert, P. M., & Burford, M. A. (2017). Globally Changing Nutrient Loads and Harmful Algal Blooms: Recent Advances, New Paradigms, and Continuing Challenges. *Oceanography*, *30*(1), 58–69.

Glibert, P. M., Icarus Allen, J., Artioli, Y., Beusen, A., Bouwman, L., Harle, J., Holmes, R., & Holt, J. (2014). Vulnerability of coastal ecosystems to changes in harmful algal bloom distribution in response to climate change: Projections based on model analysis. *Global Change Biology*, *20*(12), 3845–3858. https://doi.org/10.1111/gcb.12662

He, K., Zhang, X., Ren, S., & Sun, J. (2016). *Deep Residual Learning for Image Recognition*. 770–778. https://openaccess.thecvf.com/content_cvpr_2016/html/He_Deep_Residual_Learning_CVPR_2016_paper.html

Heil, C. A., & Steidinger, K. A. (2009). Monitoring, management, and mitigation of *Karenia* blooms in the eastern Gulf of Mexico. *Harmful Algae*, *8*(4), 611–617. https://doi.org/10.1016/j.hal.2008.11.006

Hu, C., Barnes, B. B., Qi, L., Lembke, C., & English, D. (2016). Vertical migration of *Karenia brevis* in the northeastern Gulf of Mexico observed from glider measurements. *Harmful Algae*, *58*, 59–65. https://doi.org/10.1016/j.hal.2016.07.005

Hu, C., Barnes, B., Qi, L., & Corcoran, A. (2015). A Harmful Algal Bloom of *Karenia brevis* in the Northeastern Gulf of Mexico as Revealed by MODIS and VIIRS: A Comparison. *Sensors*, *15*(2), 2873–2887. https://doi.org/10.3390/s150202873

Hu, C., & Feng, L. (2016). Modified MODIS fluorescence line height data product to improve image interpretation for red tide monitoring in the eastern Gulf of Mexico. *Journal of Applied Remote Sensing*, *11*(1), 012003. https://doi.org/10.1117/1.JRS.11.012003

Hu, C., Feng, L., Lee, Z., Davis, C. O., Mannino, A., McClain, C. R., & Franz, B. A. (2012). Dynamic range and sensitivity requirements of satellite ocean color sensors: Learning from the past. *Applied Optics*, *51*(25), 6045–6062. https://doi.org/10.1364/AO.51.006045

Hu, C., Muller-Karger, F., Taylor, C., Carder, K., Kelble, C., Johns, E., & Heil, C. (2005). Red tide detection and tracing using MODIS fluorescence data: A regional example in SW Florida coastal waters. *Remote Sensing of Environment*, *97*(3), 311–321. https://doi.org/10.1016/j.rse.2005.05.013

Hu, C., Murch, B., Corcoran, A. A., Zheng, L., Barnes, B. B., Weisberg, R. H., Atwood, K., & Lenes, J. M. (2016). Developing a smart semantic web with linked data and models for near-real-time monitoring of red tides in the eastern Gulf of Mexico. *IEEE Systems Journal*, *10*(3), 1282–1290. https://doi.org/10.1109/JSYST.2015.2440782

Hu, C., Yao, Y., Cannizzaro, J. P., Garrett, M., Harper, M., Markley, L., Villac, C., & Hubbard, K. (2022). *Karenia brevis* bloom patterns on the west Florida shelf between 2003 and 2019: Integration of field and satellite observations. *Harmful Algae*, *117*, 102289. https://doi.org/10.1016/j.hal.2022.102289

Kim, S. M., Shin, J., Baek, S., & Ryu, J.-H. (2019). U-Net Convolutional Neural Network Model for Deep Red Tide Learning Using GOCI. *Journal of Coastal Research*, *90*(sp1), 302. https://doi.org/10.2112/SI90-038.1

Kirkpatrick, B., Fleming, L. E., Squicciarini, D., Backer, L. C., Clark, R., Abraham, W., Benson, J., Cheng, Y. S., Johnson, D., Pierce, R., Zaias, J., Bossart, G. D., & Baden, D. G. (2004). Literature review of Florida red tide: Implications for human health effects. *Harmful Algae*, *3*(2), 99–115. https://doi.org/10.1016/j.hal.2003.08.005

Krizhevsky, A., Sutskever, I., & Hinton, G. E. (2017). ImageNet classification with deep convolutional neural networks. *Communications of the ACM*, *60*(6), 84–90. https://doi.org/10.1145/3065386

Kruse, F. A., Lefkoff, A. B., Boardman, J. W., Heidebrecht, K. B., Shapiro, A. T., Barloon, P. J., & Goetz, A. F. H. (1993). The spectral image processing system (SIPS)—Interactive visualization and analysis of imaging spectrometer data. *Remote Sensing of Environment*, *44*(2–3), 145–163.

Lecun, Y., Bottou, L., Bengio, Y., & Haffner, P. (1998). Gradient-based learning applied to document recognition. *Proceedings of the IEEE*, *86*(11), 2278–2324. https://doi.org/10.1109/5.726791

Luis, K., Köhler, P., Frankenberg, C., & Gierach, M. (2023). First light demonstration of red solar induced fluorescence for Harmful Algal Bloom monitoring. *Geophysical Research Letters*, *50*(13), e2022GL101715. https://doi.org/10.1029/2022GL101715

Morel, A. (1988). Optical modeling of the upper ocean in relation to its biogenous matter content (case I waters). *Journal of Geophysical Research: Oceans*, *93*(C9), 10749–10768. https://doi.org/10.1029/JC093iC09p10749

Qi, L., Hu, C., Barnes, B. B., & Lee, Z. (2017). VIIRS captures phytoplankton vertical migration in the NE Gulf of Mexico. *Harmful Algae*, *66*, 40–46. https://doi.org/10.1016/j.hal.2017.04.012

Qi, L., Hu, C., Cannizzaro, J., Corcoran, A. A., English, D., & Le, C. (2015). VIIRS observations of a *Karenia brevis* bloom in the northeastern Gulf of Mexico in the absence of a fluorescence Band. *IEEE Geoscience and Remote Sensing Letters*, *12*(11), 2213–2217. https://doi.org/10.1109/LGRS.2015.2457773

Qi, L., Yao, Y., English, D. E., Ma, R., Luft, J., & Hu, C. (2021). Remote sensing of brine shrimp cysts in salt lakes. *Remote Sensing of Environment*, *266*, 112695. https://doi.org/10.1016/j.rse.2021.112695

Ronneberger, O., Fischer, P., & Brox, T. (2015). U-Net: Convolutional Networks for Biomedical Image Segmentation. In N. Navab, J. Hornegger, W. M. Wells, & A. F. Frangi (Eds.), *Medical Image Computing and Computer-Assisted Intervention – MICCAI 2015* (pp. 234–241). Springer International Publishing. https://doi.org/10.1007/978-3-319-24574-4_28

Schofield, O., Grzymski, J., Bissett, W. P., Kirkpatrick, G. J., Millie, D. F., Moline, M., & Roesler, C. S. (1999). Optical Monitoring and Forecasting Systems for Harmful Algal Blooms: Possibility or Pipe Dream? *Journal of Phycology*, *35*(6), 1477–1496. https://doi.org/10.1046/j.1529-8817.1999.3561477.x

Schofield, O., Kerfoot, J., Mahoney, K., Moline, M., Oliver, M., Lohrenz, S., & Kirkpatrick, G. (2006). Vertical migration of the toxic dinoflagellate *Karenia brevis* and the impact on ocean optical properties. *Journal of Geophysical Research: Oceans*, *111*(C6). https://doi.org/10.1029/2005JC003115

Shin, J., Khim, B.-K., Jang, L.-H., Lim, J., & Jo, Y.-H. (2022). Convolutional neural network model for discrimination of harmful algal bloom (HAB) from non-HABs using Sentinel-3 OLCI imagery. *ISPRS Journal of Photogrammetry and Remote Sensing*, *191*, 250–262. https://doi.org/10.1016/j.isprsjprs.2022.07.012

Soto, I. M., Cannizzaro, J., Muller-Karger, F. E., Hu, C., Wolny, J., & Goldgof, D. (2015). Evaluation and optimization of remote sensing techniques for detection of *Karenia brevis* blooms on the West Florida Shelf. *Remote Sensing of Environment*, *170*, 239–254. https://doi.org/10.1016/j.rse.2015.09.026

Stehman, S. V. (1997). Selecting and interpreting measures of thematic classification accuracy. *Remote Sensing of Environment*, *62*(1), 77–89. https://doi.org/10.1016/S0034-4257(97)00083-7

Steidinger, K. A. (2009). Historical perspective on *Karenia brevis* red tide research in the Gulf of Mexico. *Harmful Algae*, *8*(4), 549–561. https://doi.org/10.1016/j.hal.2008.11.009

Stumpf, R. P. (2001). Applications of Satellite Ocean Color Sensors for Monitoring and Predicting Harmful Algal Blooms. *Human and Ecological Risk Assessment: An International Journal*, *7*(5), 1363–1368. https://doi.org/10.1080/20018091095050

Stumpf, R. P., Culver, M. E., Tester, P. A., Tomlinson, M., Kirkpatrick, G. J., Pederson, B. A., Truby, E., Ransibrahmanakul, V., & Soracco, M. (2003). Monitoring *Karenia brevis* blooms in the Gulf of Mexico using satellite ocean color imagery and other data. *Harmful Algae*, *2*(2), 147–160. https://doi.org/10.1016/S1568-9883(02)00083-5

Tester, P. A., Shea, D., Kibler, S. R., Varnam, S. M., Black, M. D., & Wayne Litaker, R. (2008). Relationships among water column toxins, cell abundance and chlorophyll concentrations during *Karenia brevis* blooms. *Continental Shelf Research*, *28*(1), 59–72. https://doi.org/10.1016/j.csr.2007.04.007

Tester, P. A., & Steidinger, K. A. (1997). *Gymnodinium breve* red tide blooms: Initiation, transport, and consequences of surface circulation. *Limnology and Oceanography*, *42*(5part2), 1039–1051. https://doi.org/10.4319/lo.1997.42.5_part_2.1039

Tester, P. A., & Stumpf, R. P. (1998). Phytoplankton blooms and remote sensing: What is the potential for early warning. *Journal of Shellfish Research*, *17*, 1469–1472.

Thuillier, G., Hersé, M., Labs, D., Foujols, T., Peetermans, W., Gillotay, D., Simon, P. C., & Mandel, H. (2003). The solar spectral irradiance from 200 to 2400 nm as measured by the SOLSPEC spectrometer from the ATLAS 1-2-3 and EURECA missions. *Solar Physics*, *214*, 1–22.

Tomlinson, M. C., Stumpf, R. P., Ransibrahmanakul, V., Truby, E. W., Kirkpatrick, G. J., Pederson, B. A., Vargo, G. A., & Heil, C. A. (2004). Evaluation of the use of SeaWiFS imagery for detecting *Karenia brevis* harmful algal blooms in the eastern Gulf of Mexico. *Remote Sensing of Environment*, *91*(3–4), 293–303. https://doi.org/10.1016/j.rse.2004.02.014

Tomlinson, M. C., Wynne, T. T., & Stumpf, R. P. (2009). An evaluation of remote sensing techniques for enhanced detection of the toxic dinoflagellate, *Karenia brevis*. *Remote Sensing of Environment*, *113*(3), 598–609. https://doi.org/10.1016/j.rse.2008.11.003

Tyler, M. A., & Stumpf, R. P. (1989). Feasibility of using satellites for detection of kinetics of small phytoplankton blooms in estuaries: Tidal and migrational effects. *Remote Sensing of Environment*, *27*(3), 233–249. https://doi.org/10.1016/0034-4257(89)90085-0

Wang, M., & Hu, C. (2021). Satellite remote sensing of pelagic Sargassum macroalgae: The power of high resolution and deep learning. *Remote Sensing of Environment*, *264*, 112631. https://doi.org/10.1016/j.rse.2021.112631

Wang, M., Jiang, L., Mikelsons, K., & Liu, X. (2021). Satellite-derived global chlorophyll-a anomaly products. *International Journal of Applied Earth Observation and Geoinformation*, *97*, 102288. https://doi.org/10.1016/j.jag.2020.102288

Wang, M., Liu, X., Jiang, L., & Son, S. (2017). *Visible Infrared Imaging Radiometer Suite Ocean Color Products. VIIRS Ocean Color Algorithm Theoretical Basis Document*. NOAA/NESDIS/STAR: Maryland, USA, 2017.

Weisberg, R. H., Liu, Y., Lembke, C., Hu, C., Hubbard, K., & Garrett, M. (2019). The coastal ocean circulation influence on the 2018 West Florida Shelf *K. brevis* red tide bloom. *Journal of Geophysical Research: Oceans*, *124*(4), 2501–2512. https://doi.org/10.1029/2018JC014887

Xiao, X., Lian, S., Luo, Z., & Li, S. (2018). Weighted Res-UNet for High-Quality Retina Vessel Segmentation. *2018 9th International Conference on Information Technology in Medicine and Education (ITME)*, 327–331. https://doi.org/10.1109/ITME.2018.00080

Yao, Y., Hu, C., & Barnes, B. B. (2023). Mysterious increases of whiting events in the Bahama Banks. *Remote Sensing of Environment*, *285*, 113389. https://doi.org/10.1016/j.rse.2022.113389

Figures

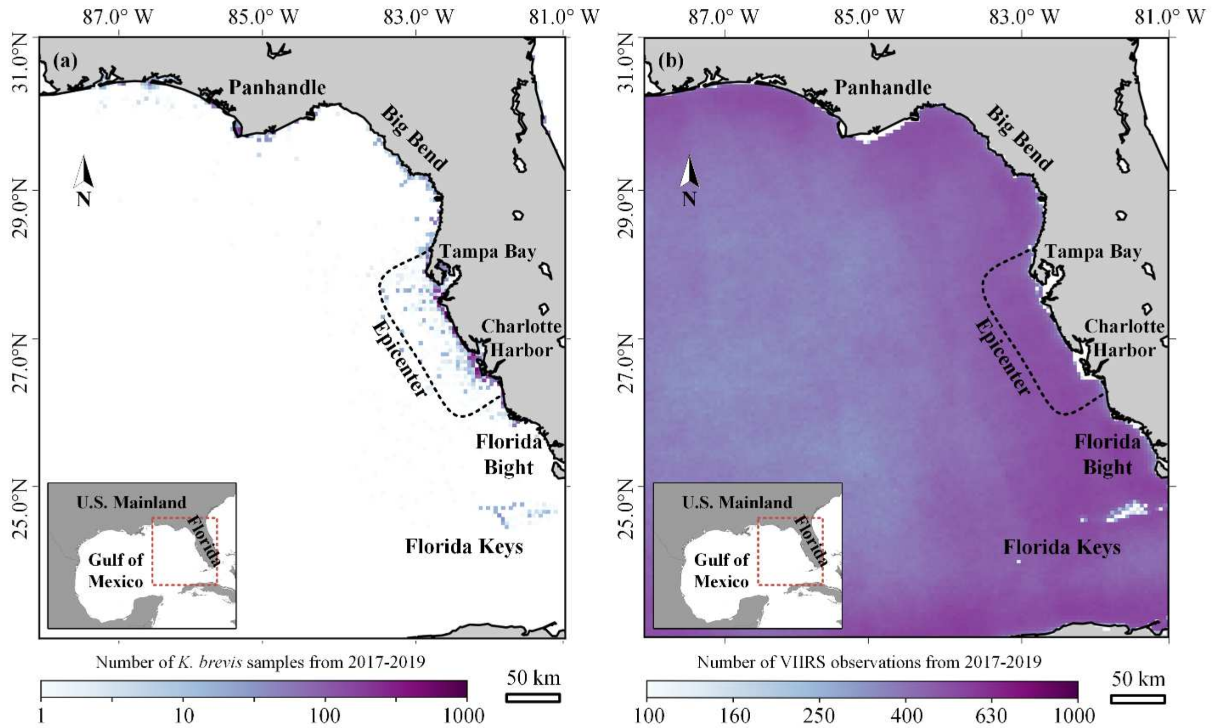

Fig. 1. The West Florida Shelf is located in the eastern Gulf of Mexico (inset map), spanning the region west of the Florida peninsula, encompassing the Panhandle, Big Bend, Central West Florida Shelf, including Tampa Bay and Charlotte Harbor, and the Florida Keys. The number of (a) discrete *in situ K. brevis* cellular abundance observations with scale from 1–1000 and (b) valid VIIRS observations in each 5-km grid in 2017–2019 with scale from 100–1000 are shown. The number of valid MODIS observations has been shown in Hu et al. (2022). Following Weisberg et al. (2019), the region from the north of Tampa Bay to the south of Charlotte Harbor is outlined as the *K. brevis* bloom "epicenter", i.e., where most *K. brevis* blooms were found and most water samples were collected.

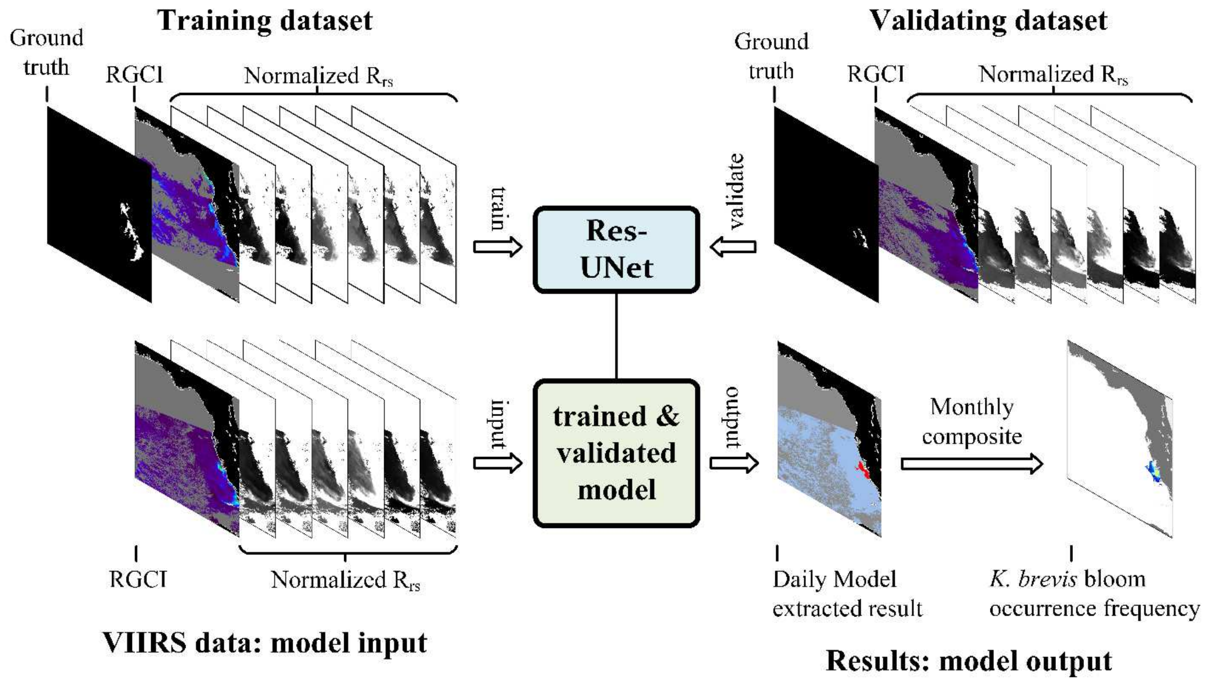

Fig. 2. Conceptual illustration of the model training, validation, and application activities conducted in this study for classifying *K. brevis* blooms in VIIRS imagery using a deep learning approach. In the top row, VIIRS "ground truth", $R_{rs}(\lambda)$, and RGCI images are used for training and validating the deep learning model. In the bottom row, the validated model was applied to VIIRS $R_{rs}(\lambda)$ and RGCI data to delineate *K. brevis* bloom patches. The pixels were classified as '*K. brevis* bloom' (red), 'non-*K. brevis* bloom' (blue), and 'no valid observation' (grey). Monthly bloom occurrence frequency maps were generated from the individual (near-daily) model extracted results.

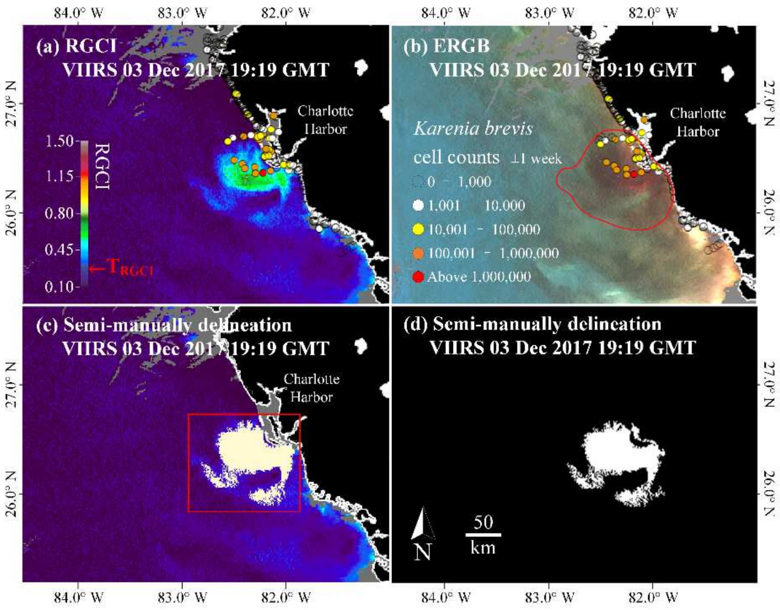

Fig. 3. "Ground truth" image preparation steps for the training the DL model. In (a), VIIRS RGCI is overlaid with *K. brevis* field sample data (±1 week) (shown in colored circles). The spatially coherent high-RGCI patch in (a) and reddish-dark patch in the VIIRS ERGB composite image (b) that is collocated with high *K. brevis* cell counts (>100,000 cells L^{-1}) suggest that this is a *K. brevis* bloom patch. A crude outline is manually drawn over the patch. In (c), pixels within the manual outline with RGCI values greater than the RGCI threshold (T_{RGCI} is marked on the color bar) are considered as bloom pixels. In (d), pixels in the delineated patch (*K. brevis* bloom) are marked as 1 (white), and all other pixels (non-*K. brevis* bloom) are marked as 0 (black).

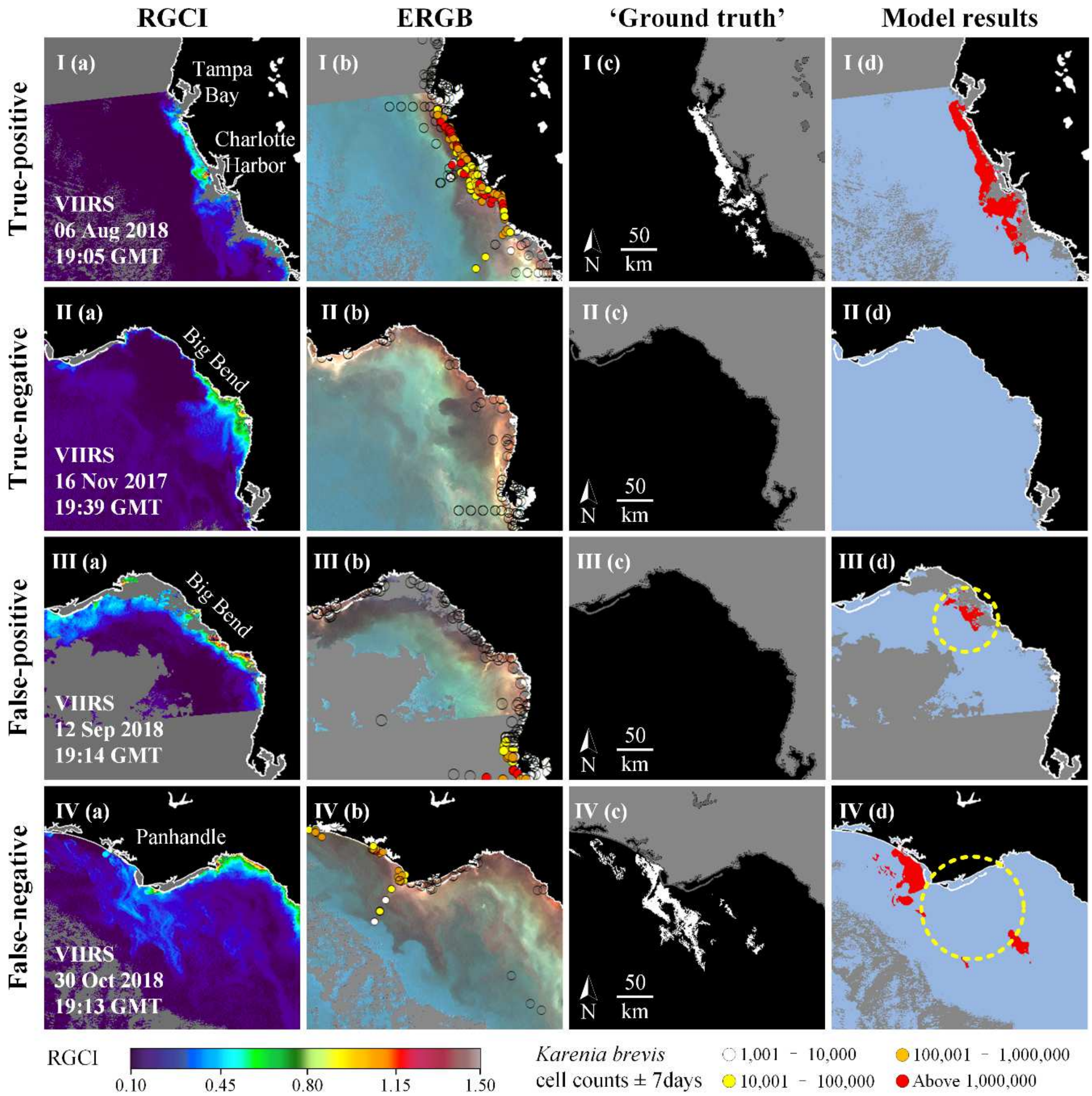

Fig. 4. Four sets of example imagery from the validation dataset. The first row (I) shows a case with true-positive results. The second row (II) shows a case with true-negative results. The third row (III) shows the false-positive results, and the fourth row (IV) shows the false-negative results (poor results are circled in dashed lines) as compared with the "ground truth" delineation in (c). Imagery shown include: (a) VIIRS RGCI; (b) VIIRS ERGB-composite images with field *K. brevis* cell count data overlaid, cell counts less than 1000 show as transparent circles; (c) VIIRS semi-objectively delineated results, and (d) VIIRS DL model extracted results with red, blue, and grey representing *K. brevis* blooms, non-*K. brevis* bloom, and no valid observation or no satellite data, respectively.

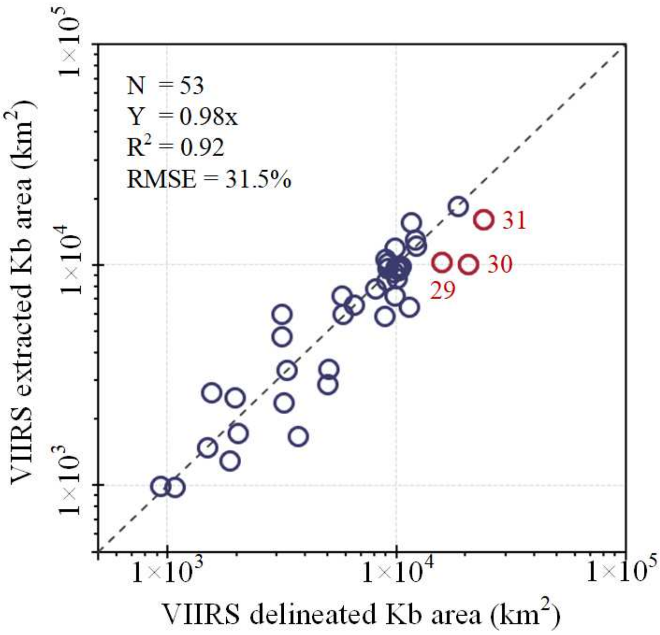

Fig. 5. Scatter plot of *K. brevis* bloom area (km^2) determined from the VIIRS delineated "ground truth" dataset (based on visual inspection of co-located VIIRS imagery and in-situ data) and trained VIIRS DL model. Red circles represent the image pairs that the bloom detected in Panhandle region on 29, 30 and 31 October 2018. Cases where neither method identified a *K. brevis* bloom are not shown.

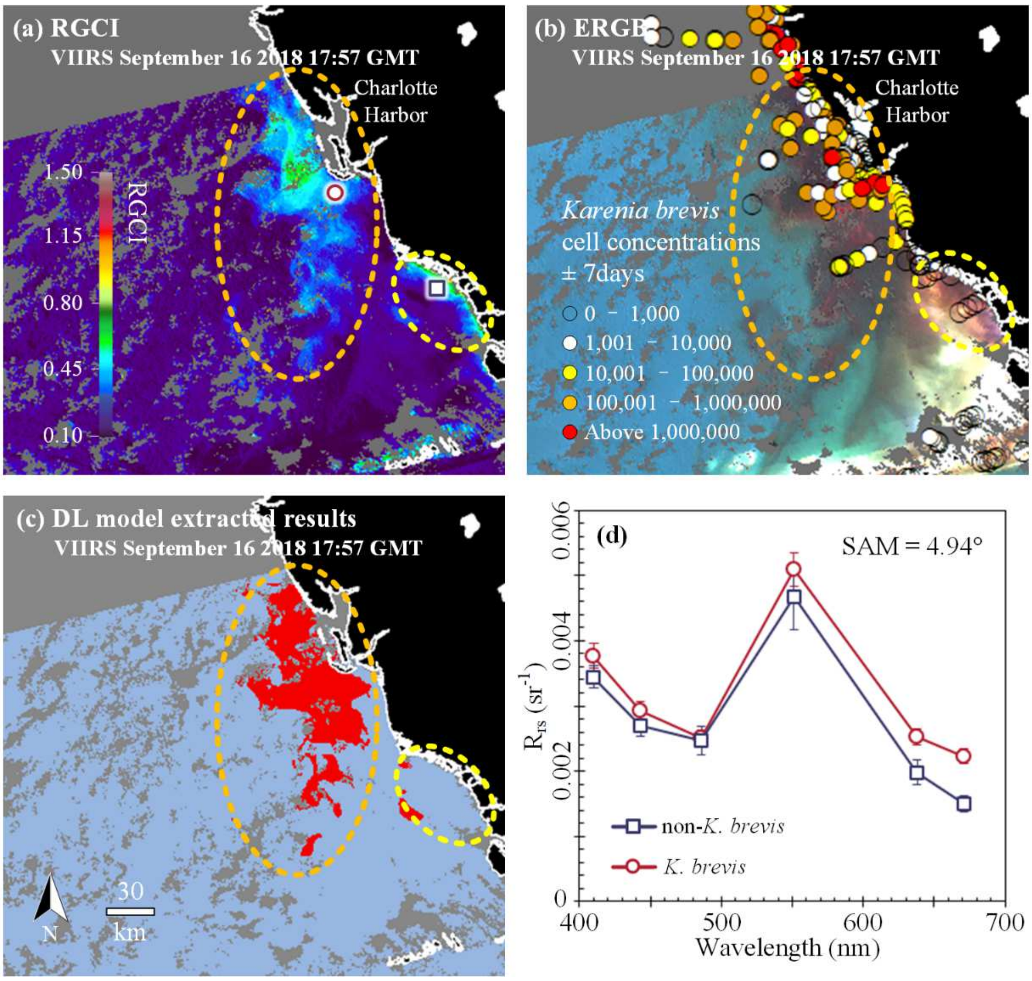

Fig. 6. The capacity of the DL model in separating *K. brevis* and non-*K. brevis* bloom patches in optically complex nearshore waters is demonstrated here using a VIIRS scene of the WFS collected on 16 September 2018 for cases of (a) VIIRS RGCI, (b) VIIRS ERGB composite image overlaid with field *K. brevis* cellular abundance data, where high RGCI values are shown to correspond to dark waters, and (c) *K. brevis* bloom patch determined from the VIIRS DL model, showing that the DL model correctly classified a high-RGCI patch (yellow dashed circle) south of the *K. bloom* patch (orange dashed circle) as non-*K. brevis* bloom. Panel (d) shows that the spectral shapes from the two locations (one in the *K. brevis* bloom and the other in the non-*K. brevis* bloom, see locations marked in (a)) are similar, yet the DL model could differentiate them.

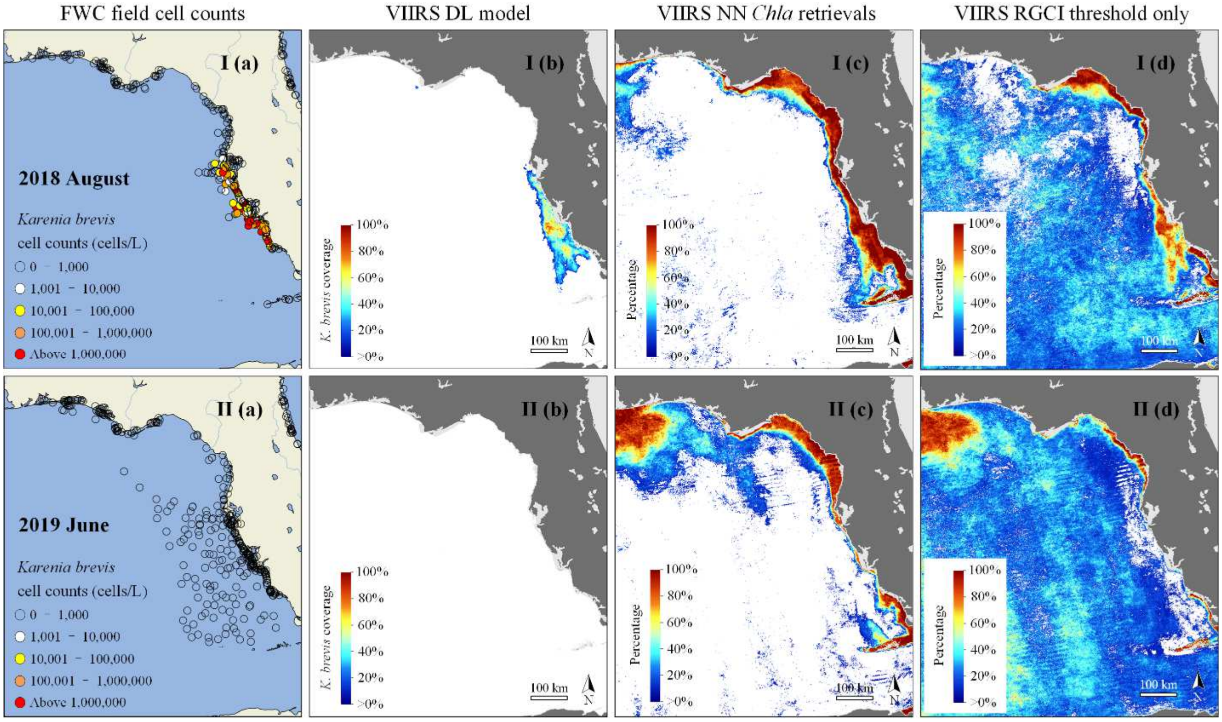

Fig. 7. Comparisons between (a) field *K. brevis* cellular abundance data (cells L^{-1}) from FWC and monthly VIIRS bloom occurrence frequency maps generated in I(a) August 2018 and II(a) June 2019 using the approaches of I(b) & II(b) DL model, I(c) & II(c) neural network model (El-Habashi et al., 2016), and I(d) & II(d) RGCI during *K. brevis* bloom (I) and non-*K. brevis* bloom (II) events. Only the DL model can correctly identify the bloom and non-bloom events.

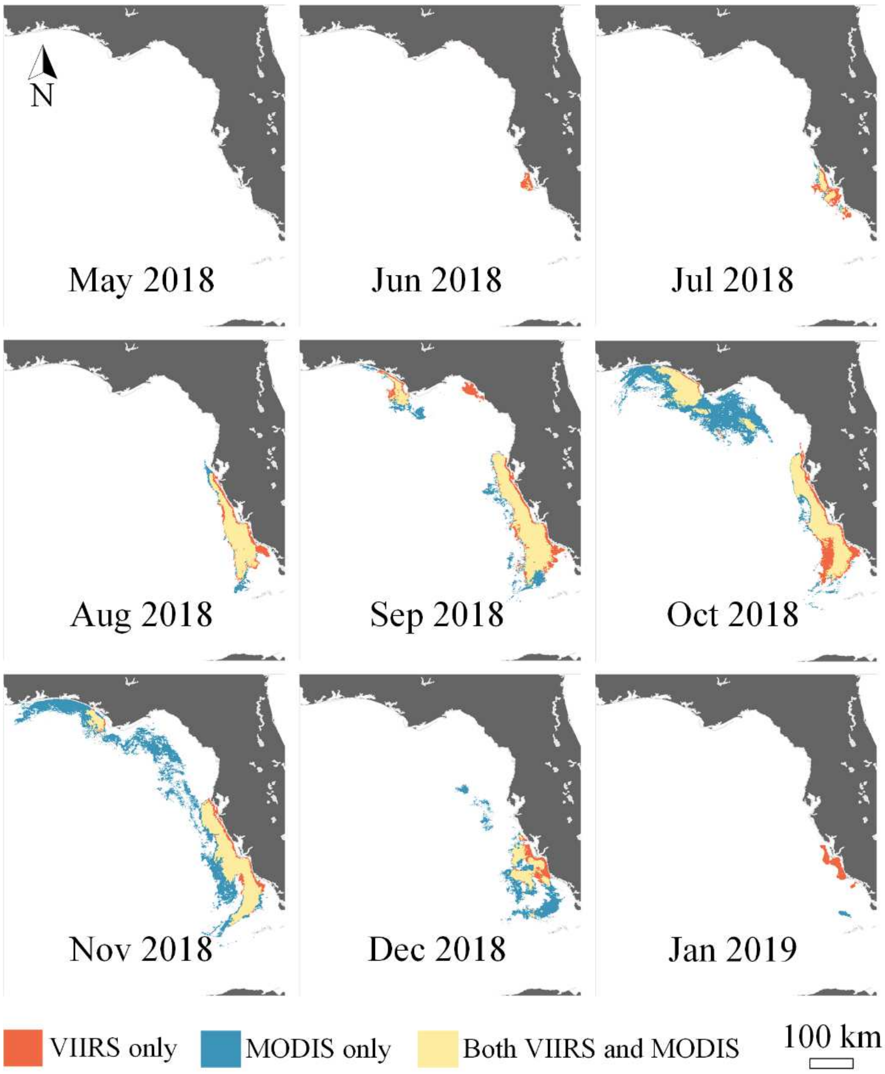

Fig. 8. Monthly *K. brevis* bloom footprint maps derived from MODIS by semi-objective delineation (Hu et al., 2022) and VIIRS using the DL model for the bloom event between mid-2018 and early-2019.

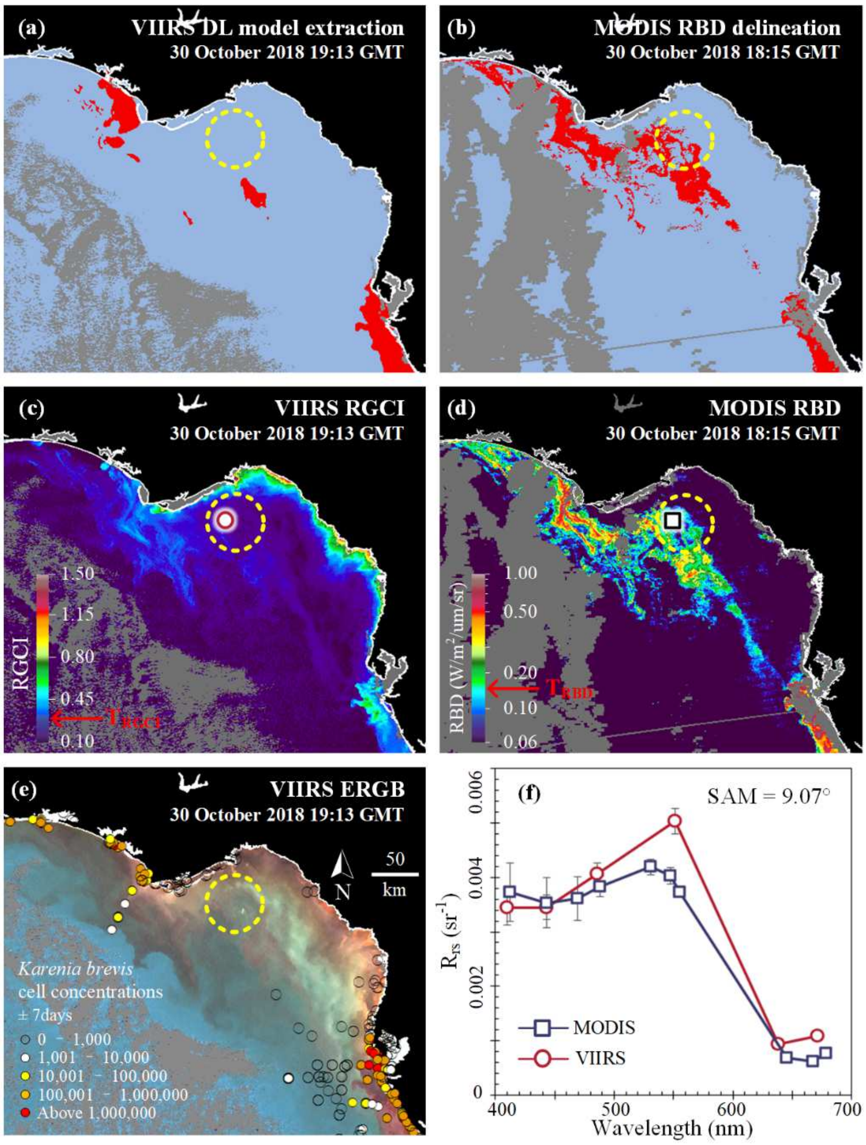

Fig. 9. The detection difference between VIIRS and MODIS in the Panhandle region on 30 October 2018 for (a) VIIRS DL model extraction results, (b) MODIS RBD delineation results based on the RBD threshold in Hu et al. (2022), (c)VIIRS RGCI image, (d) MODIS RBD image, (e) VIIRS ERGB images overlaid with *K. brevis* cell counts, and (f) VIIRS and MODIS $R_{rs}(\lambda)$ spectra from dash circled locations as noted in (d) and (e). Note that red, blue, and grey in panels (a) and (b) represent *K. brevis* blooms, non-*K. brevis* bloom, and no valid observation or no satellite data, respectively.

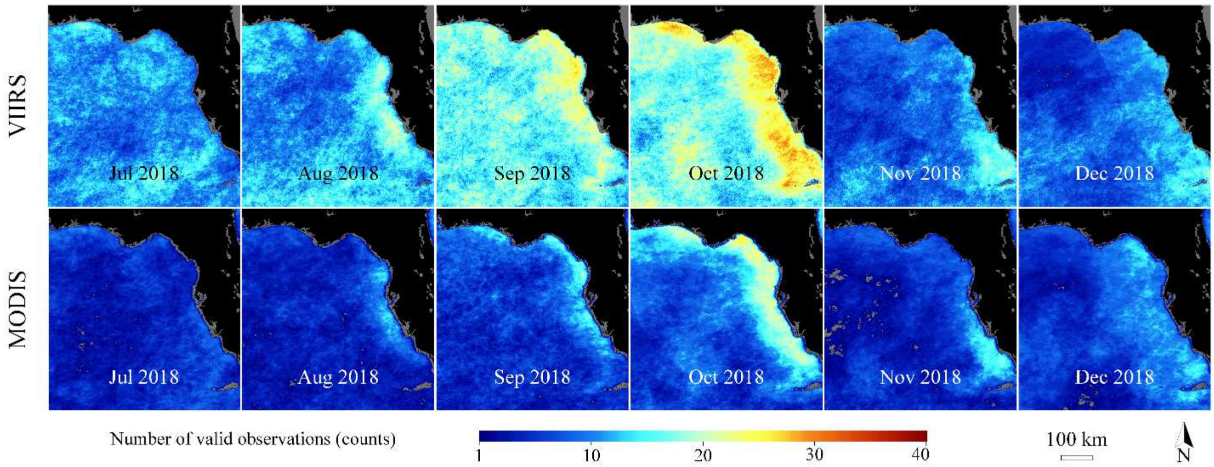

Fig. 10. Monthly images of VIIRS (top row) and MODIS (bottom row) showing the spatial distributions of number of valid observations at each 1-km location in the eastern Gulf of Mexico for each month from July to December 2018.

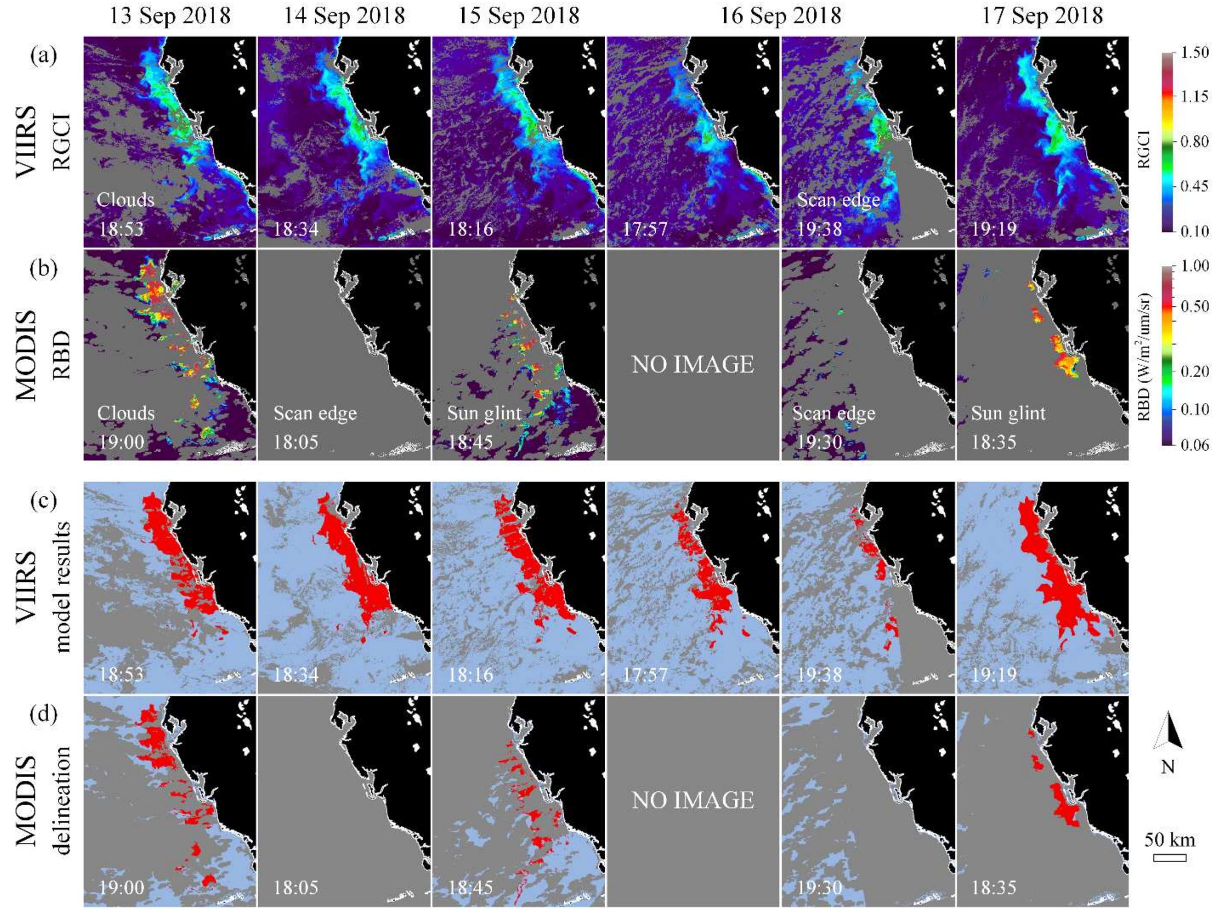

Fig. 11. An example showing the difference between VIIRS and MODIS valid observations and *K. brevis* bloom detections. The rows in (a) and (b) show the VIIRS RGCI and MODIS RBD images, respectively, over the central WFS for five consecutive days. The grey color represents no valid observation or no satellite data. The rows in (c) and (d) show their corresponding *K. brevis* bloom detection results determined with VIIRS using the DL model and MODIS by semi-objective delineation (Hu et al., 2022). Red, blue, and grey represent *K. brevis* blooms, non-*K. brevis* bloom, no valid observation or no satellite data, respectively.

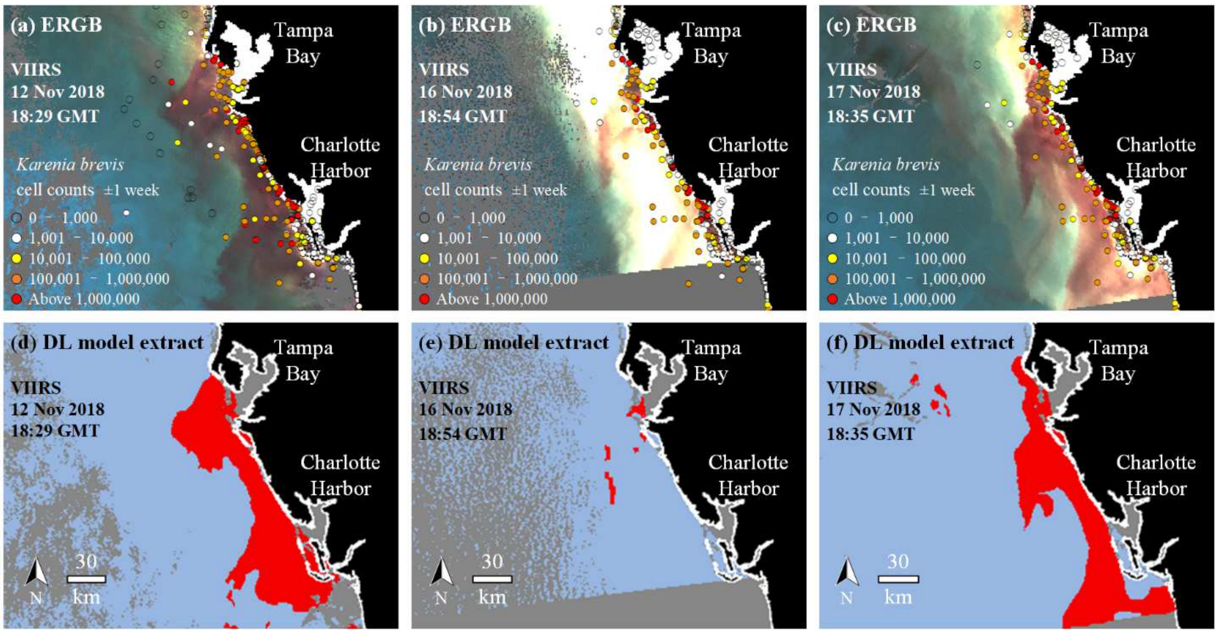

Fig. 12. An example showing how the strength of the VIIRS DL model (i.e., avoid false-positive bloom detection from sediment-rich waters) can turn into a weakness, and how such a weakness can be overcome by inspecting sequential images. Panels (a-c) are the VIIRS ERGB images in the Epicenter region overlaid with *K. brevis* cell counts, collected on 12, 16, and 17 November 2018, respectively. Panels (d-f) are the corresponding VIIRS DL model extraction results, with red, blue, and grey representing *K. brevis* bloom patches, non-*K. brevis* bloom waters, and no valid observation or no satellite data, respectively. The field data and ERGB images suggest a continuous *K. brevis* bloom in the Epicenter region in mid-November 2018. During the bloom period, the sediment resuspension event on November 16 (b) led to no bloom detection (e), but one can still safely assume the existence of similar bloom patches as in (d) and (f).

Graphical Abstract

Harmful algal blooms (HABs) of the toxic dinoflagellate *Karenia brevis*, often called red tides, occur annually on the West Florida Shelf (WFS). Detection of these HABs using satellite observations often suffers from two problems: lack of accurate algorithms to identify phytoplankton blooms in optically complex waters and patchiness (i.e., heterogeneity) of *K. brevis* cellular abundance in bloom waters. Here, to take advantage of the wide swath (3040 km) and non-saturation of the Visible Infrared Imaging Radiometer Suite (VIIRS) while realizing its disadvantage due to the lack of a fluorescence band, we develop a deep-learning (DL) convolutional neural network model to overcome the above technical challenges, especially on the spatial coherence of bloom patches. After proper training, the overall performance (i.e., F1 score) of the DL model is 89%. The results for the period of 2017 – 2019 not only demonstrate the capacity of VIIRS in HABs monitoring, but also show the value of the DL model in extracting *K. brevis* bloom patches for both near real-time applications and retrospective analysis.